

# Magnetized neutron stars with realistic equations of state and neutrino cooling

David Neilsen,<sup>1</sup> Steven L. Liebling,<sup>2</sup> Matthew Anderson,<sup>3</sup> Luis Lehner,<sup>4</sup> Evan O'Connor,<sup>5</sup> and Carlos Palenzuela<sup>5</sup><sup>1</sup>*Department of Physics and Astronomy, Brigham Young University, Provo, Utah 84602, USA*<sup>2</sup>*Department of Physics, Long Island University, Brookville, New York 11548, USA*<sup>3</sup>*Pervasive Technology Institute, Indiana University, Bloomington, Indiana 47405, USA*<sup>4</sup>*Perimeter Institute for Theoretical Physics, Waterloo, Ontario N2L 2Y5, Canada*<sup>5</sup>*Canadian Institute for Theoretical Astrophysics, Toronto, Ontario M5S 3H8, Canada*

(Received 18 March 2014; published 20 May 2014)

We incorporate realistic, tabulated equations of state into fully relativistic simulations of magnetized neutron stars along with a neutrino leakage scheme which accounts for cooling via neutrino emission. Both these improvements utilize open-source code (GR1D) and tables from the Web site [stellarcollapse.org](http://stellarcollapse.org). Our implementation makes use of a novel method for the calculation of the optical depth, which simplifies its use with distributed adaptive mesh refinement. We present various tests with and without magnetization and preliminary results both from single stars and from the merger of a binary system.

DOI: [10.1103/PhysRevD.89.104029](https://doi.org/10.1103/PhysRevD.89.104029)

PACS numbers: 04.25.D-, 04.40.Dg, 97.60.Jd

## I. INTRODUCTION

Nonvacuum, compact, binary systems (i.e., two neutron stars or a black hole paired with a neutron star) provide one of the most exciting laboratories to test fundamental aspects of diverse physics. For instance, gravitational wave observations, such as those expected from the detectors LIGO, VIRGO, and KAGRA [1–3], can shed light on the demographics of such binaries, reveal aspects of the equation of state (EoS) at nuclear densities [4–6], serve as stringent tests of General Relativity, and explore alternative gravitational theories [7–9]. Even more information will be provided by concurrent observations in both gravitational and electromagnetic bands, potentially establishing direct links between these binaries and spectacularly energetic events such as short gamma ray bursts observed already in the electromagnetic spectrum (see e.g., [10]). Additionally, these systems are expected to be prodigious producers of neutrinos and, provided they are sufficiently close, triggers for detectors such as IceCUBE and Super-Kamiokande [11]. The development of the latest generation of detectors across these channels promises exciting insights from multimessenger astronomy.

Extracting such insight from observation, however, requires theoretical predictions of these very complicated systems. And this complexity generally requires numerical simulation of a fluid coupled to relativistic gravity. Moving beyond the most simplified of fluids, those described by a polytropic EoS, further realism has been steadily achieved with an ideal gas EoS and, more recently, the adoption of generalized equations of state (e.g., [12,13]). Studies have also explored the variation of physical parameters, such as masses, mass ratios, and spin orientations and magnitudes (see [14–17]). Consideration of magnetic fields in these binaries has been pursued with either ideal magnetohydro

dynamics (MHD) [15,18–21] or resistive MHD [22], and incipient steps have considered neutrino production during the merger [23–26] or in related single-star systems [27,28] (see also [29]).

The effects of magnetic field and neutrino production and cooling play a subleading role in the dynamics of the binary during its orbiting stages. On the other hand, they can profoundly affect the outcome of the merger and its subsequent evolution. In the particular case of a binary neutron star system, to leading order, the lifetime of the remnant is determined by the individual stellar masses, the properties of the EoS, the presence of angular momentum transport mechanisms and cooling effects. If the total mass of the binary exceeds  $\approx 2.6 - 2.8M_{\odot}$ , prompt collapse to black hole is expected [23]. Otherwise a hypermassive neutron star (HMNS) is formed, supported by thermal pressure, differential rotation, and the stiffness provided by its EoS. In particular, during the merger kinetic energy is transformed into thermal energy resulting in a very hot central region (many tens of MeV) providing significant thermal pressure. The angular momentum given to the remnant from the merger provides for strong, differential rotation centrifugally supporting the concentrated mass. Thus, the rates of cooling and angular momentum transport can have a decisive impact on the onset of delayed black hole formation.

The timescale associated with the transport of angular momentum due to magnetic field winding is of the order  $\tau_{\text{wind}} \approx R/v_A$  with  $R$  the HMNS radius and  $v_A \approx B/\sqrt{\rho}$  the Alfvén velocity. Simulations have found that during the merger the magnetic field strength  $B$  can increase as high as  $10^{15-16}$  G. The increase arises from the compression and winding of the magnetic field and the transfer of hydrodynamical kinetic energy to electromagnetic energy via Kelvin-Helmholtz instabilities and turbulent amplification

[18,30–33]. For typical densities, these values lead to predicted timescales of  $\tau_{\text{wind}} \approx 10\text{--}100$  ms. We note that the computational demands of both evolving for this time period and exploring the complete parameter space make such computations currently impractical. Simulations of the magneto-rotational instability, another factor resulting in the transport of angular momentum, are even more challenging. Its role in nonvacuum, compact object merger is still largely unexplored. Nevertheless, estimates indicate a timescale  $\tau_{\text{MRI}} \approx 100$  ms for magnetic field strengths of  $B \approx 10^{15}$  G. Therefore, either effect can operate within timescales  $\gtrsim 10\text{--}100$  ms and contribute to the collapse. In contrast, cooling (via radiation transport) is estimated to act on the order of seconds, and so while relatively unlikely to impact strongly the dynamics of the HMNS (except in sufficiently low mass binaries), the extreme temperatures achieved by the merger can induce a strong neutrino luminosity.

Here we describe our incorporation both of generalized EoSs and of neutrino cooling. The former is achieved by extending our MHD implementation to handle tabulated equations of state, and the latter requires adding a suitable approximation to the relevant microphysics. A complete treatment of the microphysics would generally require solving the full transport problem in three (spatial) dimensions—along with three additional dimensions for the momentum phase space—which is currently out of reach for current (and near-future) computational resources. There are various approaches to approximating transport such as the truncated moment formalism for radiative hydrodynamics [34,35] and similar work utilizing a radiative transfer code applied to the ejecta predicted by their relativistic code to produce light curves for comparison to a recent kilonova prospect [36]. Fortunately however, the late stages of compact binary mergers occur on short timescales (with the possible exception of, yet to be observed, low mass binaries) and the details of radiation transport are subleading with respect to the bulk dynamics of the system. It therefore suffices to account for the changes to energy and lepton number only locally in a *leakage* approach [37,38].

Within efforts to simulate core-collapse supernovae, codes implementing the leakage approach have been constructed, validated, and distributed publicly [39,40], and we modify one of these [39] for use within our compact binary simulations. In this scheme, the neutrino energy and lepton number emission from microphysical processes is determined via an interpolation between two limiting regimes: the diffusion limit and the free streaming limit. We maintain consistency by accounting for the energy and lepton number emission in the fluid variables. We study the effects of neutrino cooling and compare to previous work—where such work exists—for both single stars and binaries. The results indicate a robust, convergent code consistent with past work.

In Sec. II, we describe our implementation of realistic EoS and of the leakage scheme, and in Sec. III we present the results of a number of tests. We conclude in Sec. IV.

## II. IMPLEMENTATION

Our previous studies on neutron stars used a perfect fluid with an ideal equation of state with  $\Gamma = 2$ . In this paper we detail only the recent changes to our code to use finite temperature equations of state and the leakage scheme. However, we also briefly present the Einstein and fluid equations to define our notation.

### A. Evolution equations

From a physical point of view, we follow the dynamics of both gravitational and magnetohydrodynamical fields. The former is unchanged with respect to our previously described work [41]. However, the MHD equations (e.g., [42,43]) must be modified to account for the effect of neutrinos in both energy and lepton numbers. Since the leakage scheme is essentially a local calculation (the exception being the optical depth) providing lepton and energy rates of change as measured by a comoving observer, its extension to the general relativistic case is straightforward. For the sake of completeness, we describe next the basic strategy.

The Einstein equations in the presence of both matter and radiation are

$$G_{ab} = 8\pi(T_{ab} + \mathcal{R}_{ab}), \quad (1)$$

where  $T_{ab}$  is the stress energy tensor of a perfect fluid,  $\mathcal{R}_{ab}$  is the contribution from the radiation field, and we have adopted geometrized units where  $G = c = M_{\odot} = 1$ . Equation (1), coupled with appropriate prescriptions for the dynamics of  $T_{ab}$  and  $\mathcal{R}_{ab}$ , defines the system of equations. In what follows we briefly describe how each is implemented.

We solve the Einstein equations by adopting a  $3 + 1$  decomposition in terms of a spacelike foliation. The hypersurfaces that constitute this foliation are labeled by a time coordinate  $t$  with unit normal  $n^a$  and endowed with spatial coordinates  $x^i$ . We express the spacetime metric as

$$ds^2 = -\alpha^2 dt^2 + \gamma_{ij}(dx^i + \beta^i dt)(dx^j + \beta^j dt), \quad (2)$$

with  $\alpha$  the lapse function and  $\beta^i$  the shift vector. Specifically, we express the Einstein equations in terms of the BSSN-NOK formalism [44–47]. In this formulation, the metric on spatial hypersurfaces,  $\gamma_{ij}$ , is expressed in terms of a conformal factor  $\chi$  and a conformally flat metric  $\tilde{\gamma}_{ij}$

$$\gamma_{ij} = \frac{1}{\chi} \tilde{\gamma}_{ij}, \quad \chi = (\det \gamma_{ij})^{-1/3} \quad (3)$$

such that  $\det \tilde{\gamma}_{ij} = 1$ . In addition, the extrinsic curvature  $K_{ij}$  is decomposed into its trace  $K \equiv K^i_i$  and the conformal, trace-less extrinsic curvature  $\tilde{A}_{ij} = \chi(K_{ij} - \frac{1}{3}\gamma_{ij}K)$ . Finally, one introduces the conformal connection functions  $\tilde{\Gamma}^i = \tilde{\gamma}^{jk}\tilde{\Gamma}^i_{jk}$ , which are evolved as independent variables. The evolution equations are

$$\begin{aligned} \partial_t \tilde{\gamma}_{ij} &= \beta^k \partial_k \tilde{\gamma}_{ij} + \tilde{\gamma}_{ik} \partial_j \beta^k + \tilde{\gamma}_{kj} \partial_i \beta^k \\ &\quad - \frac{2}{3} \tilde{\gamma}_{ij} \partial_k \beta^k - 2\alpha \tilde{A}_{ij} \end{aligned} \quad (4)$$

$$\partial_t \chi = \beta^i \partial_i \chi + \frac{2}{3} \chi (\alpha K - \partial_j \beta^j) \quad (5)$$

$$\begin{aligned} \partial_t \tilde{A}_{ij} &= \beta^k \partial_k \tilde{A}_{ij} + \tilde{A}_{ik} \partial_j \beta^k + \tilde{A}_{kj} \partial_i \beta^k - \frac{2}{3} \tilde{A}_{ij} \partial_k \beta^k \\ &\quad + \chi [-D_i D_j \alpha + \alpha (R_{ij} - 8\pi S_{ij})]^{\text{TF}} \\ &\quad + \alpha (K \tilde{A}_{ij} - 2 \tilde{A}_{ik} \tilde{A}^k_j) \end{aligned} \quad (6)$$

$$\begin{aligned} \partial_t K &= \beta^k \partial_k K - D^i D_i \alpha \\ &\quad + \alpha \left[ \tilde{A}_{ij} \tilde{A}^{ij} + \frac{1}{3} K^2 + 4\pi (E + S) \right] \end{aligned} \quad (7)$$

$$\begin{aligned} \partial_t \tilde{\Gamma}^i &= \beta^j \partial_j \tilde{\Gamma}^i - \tilde{\Gamma}^j \partial_j \beta^i + \frac{2}{3} \tilde{\Gamma}^i \partial_j \beta^j + \tilde{\gamma}^{jk} \partial_j \partial_k \beta^i \\ &\quad + \frac{1}{3} \tilde{\gamma}^{ij} \partial_j \partial_k \beta^k - 2 \tilde{A}^{ij} \partial_j \alpha \\ &\quad + 2\alpha \left( \tilde{\Gamma}^i_{jk} \tilde{A}^{jk} - \frac{3}{2\chi} \tilde{A}^{ij} \partial_j \chi - \frac{2}{3} \tilde{\gamma}^{ij} \partial_j K - 8\pi \tilde{\gamma}^{ij} S_j \right). \end{aligned} \quad (8)$$

In these equations, the matter terms are defined as

$$E \equiv n_a n_b (T^{ab} + \mathcal{R}^{ab}) \quad (9)$$

$$S_i \equiv -\gamma_{ia} n_b (T^{ab} + \mathcal{R}^{ab}) \quad (10)$$

$$S_{ij} \equiv \gamma_{ia} \gamma_{jb} (T^{ab} + \mathcal{R}^{ab}). \quad (11)$$

Notice that for the problem of interest  $|\mathcal{R}^{ab}| \ll |T^{ab}|$ . This observation, together with the fact that a neutrino leakage scheme can not possibly treat the radiation stress tensor fully consistently, we choose to ignore the source-term-contribution from the radiation field to the Einstein equations.

The evolution equations are supplemented with gauge conditions. We use the “1 + log” slicing condition and the  $\Gamma$ -driver shift with the evolution equations

$$\partial_t \alpha = \lambda_1 \beta^i \partial_i \alpha - 2\alpha K \quad (12)$$

$$\partial_t \beta^i = \lambda_2 \beta^j \partial_j \beta^i + \frac{3}{4} f(\alpha) B^i \quad (13)$$

$$\partial_t B^i = \partial_t \tilde{\Gamma}^i - \eta B^i + \lambda_3 \beta^j \partial_j B^i - \lambda_4 \beta^j \partial_j \tilde{\Gamma}^i. \quad (14)$$

Here  $f(\alpha)$  is an arbitrary function and  $\lambda_1, \lambda_2, \lambda_3, \lambda_4$ , and  $\eta$  are parameters that can be chosen for different types of initial data. Our simulations are performed with the choice  $f(\alpha) = \lambda_i = 1$  and  $\eta \approx 3.5/M$ , where  $M$  is the total mass of the system. Finally, during the evolution the algebraic constraints,

$$\det \tilde{\gamma}_{ij} = 1, \quad \tilde{A}^i_i = 0, \quad (15)$$

are enforced at every step.

## B. Matter

For the matter source we consider a perfect fluid with stress energy tensor given by

$$T_{ab} = h u_a u_b + P g_{ab} + F_{ac} F_b^c - \frac{1}{4} g_{ab} F_{cd} F^{cd}. \quad (16)$$

where  $h$  is the total enthalpy  $h = \rho(1 + \epsilon) + P$ , and  $\{\rho, \epsilon, u^a, P\}$  are the rest mass energy density, specific internal energy, four-velocity and pressure, respectively, and  $F_{ab}$  the Faraday tensor (absorbing a factor  $1/\sqrt{4\pi}$  in its definition). Provided an equation of state of the form  $P = P(\rho, \epsilon, Y_e)$  and a relativistic Ohm's law, the equations determining the magnetized matter dynamics are obtained from suitable conservation laws. We here adopt the ideal MHD approximation (which states that the fluid is described by an isotropic Ohm's law with perfect conductivity, so that the electric field vanishes in the fluid's frame  $F_{ab} u^b = 0$ ) which provides a simple, realistic approach reducing the number of relevant fields to describe electromagnetic effects in the system.

The resulting system of equations is

$$\nabla_a T_b^a = \mathcal{G}_b \quad (17)$$

$$\nabla^a (T_{ab} n^b) = 0 \quad (18)$$

$$\nabla_a (Y_e \rho u^a) = \rho R_Y \quad (19)$$

$$\nabla_a {}^* F^{ab} = 0. \quad (20)$$

These equations state the conservation laws for the stress-energy tensor, matter and lepton number, respectively, where  $Y_e$  is the electron fraction, the ratio of electrons to baryons. In the absence of lepton source terms, Eq. (19) follows closely the conservation law for the rest mass density, i.e.,  $Y_e$  is a mass scalar. The sources  $\mathcal{G}_a$  ( $\equiv -\nabla_c \mathcal{R}_a^c$ ) and  $R_Y$  are the radiation four-force density and lepton sources which are determined via the leakage scheme.

### 1. GR-Hydro equations

Examining the equations for the matter, Eqs. (17)–(20), a few observations are in order. On the one hand, the implementation of the equations for the magnetic field need not be modified with respect to our previous work (e.g., [48]) as they are neither directly coupled to the neutrino evolution nor do they depend on the fluid's equation of state. On the other hand, changes to the implementation of the fluid equations are required. In what follows we describe those modifications.

Recall the 3 + 1 decomposition of the fluid equations as presented in [42]. The relevant expressions of the projections with respect to  $n^a$  (parallel and orthogonal) can be written in terms of the source  $\mathcal{G}_a$  as

$$0 = -n^a \partial_a E + KE - \frac{1}{\alpha^2} D_a (\alpha^2 S^a) + (\perp T)^{ab} K_{ab} - \mathcal{G}_a n^a \quad (21)$$

$$0 = h_{bc} \left[ -n^a \partial_a S^b + KS^b + 2S^a K_a^b - \frac{1}{\alpha} S^a \partial_a \beta^b - \frac{1}{\alpha} D_a (\alpha (\perp T)^{ab}) - \frac{\partial^b \alpha}{\alpha} E + \mathcal{G}^c \right]. \quad (22)$$

Finally, we define the Lorentz factor and the three-velocity as

$$W \equiv -n^a u_a, \quad v^i \equiv \frac{1}{W} (\perp u)^i. \quad (23)$$

The fluid equations of motion are written in balance law form

$$\partial_t \mathbf{u} + \partial_i \mathbf{f}^i(\mathbf{u}) = \mathbf{s}(\mathbf{u}) \quad (24)$$

by defining the *conservative* variables. These variables are densitized using the 3-metric determinant  $\sqrt{\gamma}$  as

$$\tilde{D} \equiv \sqrt{\gamma} \rho W \quad (25)$$

$$\tilde{S}_i \equiv \sqrt{\gamma} [(hW^2 + B^2)v_i - (B^j v_j)B_i] \quad (26)$$

$$\tilde{\tau} \equiv \sqrt{\gamma} \left[ hW^2 + B^2 - P - \frac{1}{2} \left( (B^i v_i)^2 + \frac{B^2}{W^2} \right) \right] \quad (27)$$

$$\tilde{B}^i \equiv \sqrt{\gamma} B^i \quad (28)$$

$$\tilde{Y}_e \equiv \tilde{D} Y_e. \quad (29)$$

The leakage scheme provides the fluid rest frame energy sink  $\mathcal{Q}$  and lepton sink/source  $R_Y$  due to neutrino processes.  $R_Y$  is the source term for a scalar quantity and therefore is the same in all frames. We express the source term for the energy and momentum in an arbitrary frame as

$$\mathcal{G}_a = \mathcal{Q} u_a. \quad (30)$$

Since the effect of neutrino pressure is small [26] and difficult to accurately capture with a neutrino leakage scheme, we ignore its contribution in the fluid rest frame. Now, defining  $\mathcal{H} \equiv n^a \mathcal{G}_a = -\mathcal{Q}W$  and  $\mathcal{H}_b \equiv h_{bc} \mathcal{G}^c = \mathcal{Q}W v_b$ , the modified relativistic MHD equations become

$$\partial_t \tilde{D} + \partial_i \left[ \alpha \tilde{D} \left( v^i - \frac{\beta^i}{\alpha} \right) \right] = 0 \quad (31)$$

$$\begin{aligned} \partial_t \tilde{S}_j + \partial_i \left[ \sqrt{-g} \left( (\perp T)^i_j - \frac{\beta^i}{\alpha} S_j \right) \right] \\ = \sqrt{-g} \left[ {}^3\Gamma_{ab}^i (\perp T)^a_i + \frac{1}{\alpha} S_a \partial_b \beta^a - \frac{1}{\alpha} \partial_b \alpha E + \mathcal{H}_b \right] \end{aligned} \quad (32)$$

$$\begin{aligned} \partial_t \tilde{\tau} + \partial_i \left[ \alpha \left( \tilde{S}^i - \tilde{D} v^i - \frac{\beta^i}{\alpha} \tilde{\tau} \right) \right] \\ = \sqrt{-g} \left[ (\perp T)^{ab} K_{ab} - \frac{1}{\alpha} S^a \partial_a \alpha - \mathcal{H} \right] \end{aligned} \quad (33)$$

$$\partial_t \tilde{Y}_e + \partial_i \left[ \alpha \tilde{Y}_e \left( v^i - \frac{\beta^i}{\alpha} \right) \right] = \frac{\alpha}{W} \tilde{D} R_Y \quad (34)$$

$$\begin{aligned} \partial_t \tilde{B}^i + \partial_j \left[ \left( v^j - \frac{\beta^j}{\alpha} \right) \tilde{B}^i - \left( v^i - \frac{\beta^i}{\alpha} \right) \tilde{B}^j \right] \\ = -\alpha \sqrt{\gamma} \gamma^{ij} \partial_j \psi \end{aligned} \quad (35)$$

$$\partial_t \psi = -c_h^2 \frac{\alpha}{\sqrt{\gamma}} \partial_i \tilde{B}^i - \alpha c_r^2 \psi \quad (36)$$

where

$$\begin{aligned} (\perp T)^i_j = v^i S_j + P h^i_j - \frac{1}{W^2} \left[ B^i B_j - \frac{1}{2} h^i_j B^2 \right] \\ - (B^k v_k) \left[ B^i v_j - \frac{1}{2} h^i_j B^m v_m \right]. \end{aligned} \quad (37)$$

Notice that the evolution equation for  $\tilde{B}^i$  contains a scalar field ( $\psi$ ) contribution which is introduced to control the non-monopole constraint. This ‘‘divergence cleaning method’’ damps constraint violations via a damped, wave equation for the evolution of  $\psi$  [42,49].

Notice also that this system of equations is strongly hyperbolic. It contains the minimum couplings with the solenoidal constraint and includes a damping term. The terms in the right hand sides are treated as sources, and their derivatives are calculated with centered finite difference (second order). A small amount of numerical dissipation is added both to  $\{\tilde{B}^i, \psi\}$ . We have found numerically that an efficacious choice is  $c_h = 0.1$ ,  $c_r \approx 2/\sqrt{M}$  (where  $M$  is again the total mass of the system).

## C. Equations of state

### 1. Finite temperature EoS tables

Neutrino interaction rates depend sensitively on the matter temperature and composition. Therefore, in order to model the effect of neutrinos with reasonable accuracy, we require an equation of state beyond that of a polytrope or an ideal gas. We use publicly available EoS tables from <http://www.stellarcollapse.org> and described in O'Connor and Ott (2010) [39]. We have rewritten some of the library routines for searching the table to make them faster and more robust. In this paper we use the Shen-Horowitz-Teige (SHT) [50] EoS with the NL3 relativistic mean-field parametrization, the Lattimer-Swesty (LS) [51] EoS with  $K = 220$  MeV, and the H. Shen (HS) [52] for the single neutron star simulations, and the HS EoS for the neutron star binary.

### 2. The primitive solver

High-resolution shock-capturing schemes integrate the fluid equations in conservation form for the conservative variables, while the fluid equations are written in a mixture of conserved and primitive variables. It is well known that the calculation of primitive variables from conserved variables for relativistic fluids requires solving a transcendental set of equations. Our method for solving these equations with a finite-temperature EoS is a modification of the algorithm that we use for the ideal gas EoS; the most significant change being that the internal energy must be calculated separately from the pressure using the table. We write the transcendental equations in terms of the new variable

$$x \equiv hW^2, \quad (38)$$

where  $h$  is the *total* enthalpy  $h = \rho(1 + \epsilon) + P$ , and calculate  $Y_e$  from the evolution variables  $\tilde{Y}_e/\tilde{D}$ . Then, using data from the previous time step to calculate an initial guess for  $x$ , we iteratively solve these equations for  $x$ :

- (1) From the equation for  $S^i S_i$ , calculate

$$\hat{W}^{-2} = 1 - \frac{(2x + B^2)B^i S_i + x^2 S^2}{(x(x + B^2))^2}.$$

- (2) From the definition of  $D$ , calculate

$$\hat{\rho} = \frac{D}{\hat{W}}.$$

- (3) From the definition of  $\tau$ , calculate

$$\hat{P} = x - (\tau + D) + B^2 - \frac{1}{2} \left[ \left( \frac{B^i S_i}{x} \right)^2 + \frac{B^2}{\hat{W}^2} \right].$$

- (4) From the definition of the total enthalpy, calculate

$$\hat{\epsilon} = \left( \frac{x}{\hat{W}^2} - \hat{P} \right) \frac{\hat{W}}{D} - 1.$$

- (5) Use the EoS table to calculate the temperature  $\hat{T}$  from  $\hat{\epsilon}(\hat{\rho}, \hat{T}, Y_e)$ .
- (6) Use the EoS table to calculate  $P(\hat{\rho}, \hat{T}, Y_e)$ .
- (7) Update the guess for  $x$  by solving the equation  $f(x) = 0$  using the Brent method, with (again, the definition of  $\tau$ )

$$f(x) = x - P(\hat{\rho}, \hat{T}, Y_e) - \frac{1}{2} \left[ \left( \frac{B^i S_i}{x} \right)^2 + \frac{B^2}{\hat{W}^2} \right] + B^2 - (\tau + D).$$

The root of  $f(x) = 0$  from Step 7 becomes the new guess for  $x$ , and this process is repeated iteratively until the solution for  $x$  converges to a specified tolerance. One advantage of this algorithm is that  $f(x)$  is a function of a single variable, and, in contrast to root solving for multiple variables, robust methods can be used to find any root that can be bracketed.

Because of numerical error, a solution to these equations may either fall outside the physical range for the primitive variables, or a real solution for  $x$  may not exist. The solutions for  $\rho$ ,  $T$ , and  $Y_e$  are, at a minimum, restricted to values in the table, and they are reset to new values (the minimum allowed value plus ten percent) if necessary. A separate floor value for the density is also set. In anticipation of comparing this work with evolutions of magnetized stars in the future, we choose a density floor appropriate for magnetized stars for the neutron star binary, which is about eight orders of magnitude smaller than the initial central density of the stars. If a real solution for the primitive variables does not exist, the primitive variables are interpolated from neighboring points, and the conserved variables are reset to be consistent. If a valid interpolation stencil can not be constructed because the solver also failed at the neighboring points, then the update fails, and the run is terminated. This failure occurs very rarely and may be remedied by slightly increasing the density floor.

## D. Leakage

The leakage scheme seeks to account for (i) the changes to the (electron) lepton number and (ii) the loss of energy from the emission of neutrinos. As discussed, since the dynamical timescale for the post-merger of binary neutron star systems is relatively short, radiation momentum transport and diffusion effects are expected to be subleading. Our scheme is based on the open-source neutrino leakage scheme from [39], available at [stellarcollapse.org](http://stellarcollapse.org). At low

optical depths, the leakage scheme relies on calculating the emission rate of energy ( $Q_{\text{free}}$ ) and lepton number ( $R_{\text{free}}$ ) directly from the rates of relevant processes. We consider three species of neutrinos, represented here by:  $\nu_e$  for electron neutrinos,  $\bar{\nu}_e$  for electron antineutrinos, and  $\nu_x$  for both tau and muon neutrinos and their respective antineutrinos. As discussed in [37,38], the dominant processes are those that

- (i) produce electron flavor neutrinos and antineutrinos: charged-current, electron, and positron capture reactions  $e^+ + n \rightarrow p + \bar{\nu}_e$ ,  $e^- + p \rightarrow n + \nu_e$ .
- (ii) produce all flavors of neutrinos: electron-positron pair-annihilation  $e^+ + e^- \rightarrow \bar{\nu}_i + \nu_i$  and plasmon decay  $\gamma \rightarrow \bar{\nu}_i + \nu_i$ .

Notice that nucleon-nucleon bremsstrahlung can also be an important source of  $\nu_x$  neutrinos, dominating over electron-positron annihilation at low temperatures and high densities. We will include such a process in future work.

At high optical depths on the other hand, because the equilibrium time scales are much shorter than either neutrino diffusion or hydrodynamic time scales, neutrinos are assumed to be at their equilibrium abundances and the rates of energy loss ( $Q_{\text{diff}}$ ) and lepton loss ( $R_{\text{diff}}$ ) are taken to proceed at the diffusion timescale. The equilibrium abundances can be trivially calculated, however the calculation of the diffusion timescale is more involved as it requires the knowledge of nonlocal optical depths. The computation of these optical depths lies at the core of the leakage strategy and, because we are interested in general (nonspherically symmetric) scenarios, we describe how to compute them from the local opacities in Sec. II D 1. (We refer the reader to [39] for full details about the calculation of the local opacity and diffusion time scale.) The emission rates are then interpolated between the behavior at low and high optical depths in order to achieve an efficient way to incorporate neutrino effects that is correct in both regimes and applicable in between. In our implementation, we interpolate the energy and lepton number emission rates between these two regimes via the following formula

$$X_{\text{eff}} = \frac{X_{\text{diff}} X_{\text{free}}}{X_{\text{diff}} + X_{\text{free}}}, \quad (39)$$

where  $X$  is either  $Q$  or  $R$ .

### 1. Optical depth calculation

The usual approach to calculating the optical depth at a given point is to consider some small number of possible directions in which to integrate the opacity of the fluid. In GR1D [39], the assumption of spherical symmetry simplifies the calculation so that there are only ingoing and outgoing directions.

Refs. [23] and [26] integrate the depth along rays in the coordinate directions, although Ref. [26] adds certain diagonal rays. The depth at any given point is then the

minimum depth among the considered rays. Ref. [28] instead argues for rays that match the geometry of the problem and they therefore interpolate onto a spherical grid and considers the minimum depth among a set of radial rays.

In general, the existent algorithms necessarily involve global integrations that bring with them complexities due to multiple resolutions (from the AMR) and patches (from the domain decomposition). Instead, a more local approach that is independent of the particular symmetries of the problem is desirable. For example, one could determine the depth at any given point as a parallel circuit where the depth measures the “resistance” to the depth-free exterior [53]. The depth at each point is just the contribution to the depth to reach a neighboring point added to the inverse of the sum of the inverses of the depths of all neighboring points. Such a procedure turns the global integration into an iterated local problem. However, early experiments showed a problem with its application because the depth was generally less than that of any neighbors. Therefore, in a naive iteration scheme, the resulting depth did not adequately reflect the expected increasing optical depth with increased depth into the star.

However, an even simpler approach appears to work quite well. In this scheme, the depth at any given point is simply the sum of the depth incurred to get to a neighboring point plus the minimum depth among its neighbors. One can justify such an approach by arguing that neutrinos will explore all pathways out of the star, not just straight paths. This approach is also iterative since changes elsewhere do not immediately affect other areas, as would happen with a global integration. Physically one expects changes at the surface to take some time to propagate throughout the star. However, as noted in [39], because the depth depends on the opacity which itself depends on the depth, one expects to iterate in any case.

We have compared runs with no explicit iteration (our leakage routine is called at every Runge-Kutta step, instead of once per time step) with runs where we iterate three times and there is effectively no difference.

The computation of the optical depth appears to be an example of the eikonal problem [54]. The eikonal equation takes the form

$$|\nabla u(x)| = f(x) \quad (40)$$

for scalar functions  $u(x)$  and  $f(x)$  (see for example Ref. [55] for a fast method of solving it). Here, this equation takes the form

$$|\nabla \tau_i(x)| = \kappa_i(x) \quad (41)$$

where  $\tau_i$  is the optical depth for some species of neutrino and  $\kappa_i$  its corresponding opacity. Implementation of one of the approaches to the eikonal problem for the computation of optical depth may provide benefits, but here we simply use this formulation (the derivative of the defining integral

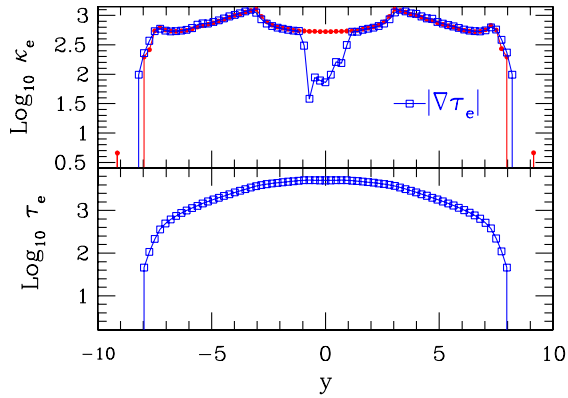


FIG. 1 (color online). *Optical depth for an isolated neutron star.* *Top:* The electron opacity  $\kappa_e$  (red solid) evolved for  $t = 1.15$  ms along the  $x$ -axis. Also shown is the magnitude of the gradient of the electron optical depth  $|\nabla\tau_e|$ . The noticeable dip in the gradient is just an effect of the post-processing used to compute the gradient and no significant feature is seen in the optical depth itself shown in the bottom panel. *Bottom:* The electron optical depth  $\tau_e$ .

for the depth) to evaluate the utility of our admittedly simplified solution.

In Fig. 1 we show both the magnitude of the gradient of the depth for electron neutrinos and compare it with its opacity for a single star. The agreement between these two indicates that even this simplified scheme is finding the correct optical depth for the given opacity.

One possible concern is that this approach is too simple to track stars in a binary and so in Fig. 2 we do the same analysis along the  $y$ -axis for a binary when the stars are suitably aligned. Once again, the features of the gradient match those of the opacity, and, in particular, the depth tracks the stars throughout their orbit.

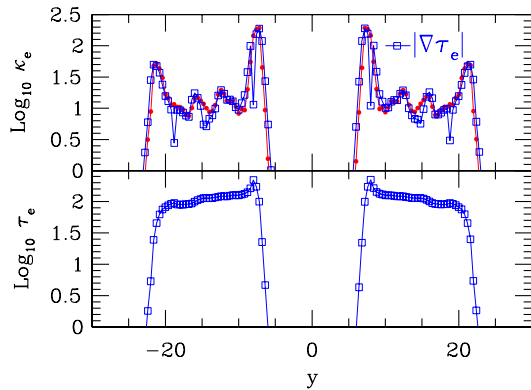


FIG. 2 (color online). *Optical depth for a binary neutron star system.* *Top:* The electron opacity  $\kappa_e$  (red solid) after a quarter orbit along the  $y$ -axis. Also shown is the magnitude of the gradient of the electron optical depth  $|\nabla\tau_e|$ . The similarity of these two quantities suggests that the optical depth algorithm adequately tracks the binary members. *Bottom:* The electron optical depth  $\tau_e$ . The binary is quite cold (initial temperature of 0.01 MeV) and so the depth is quite small.

### III. NUMERICAL RESULTS

We present initial tests and preliminary results below. A more detailed and expansive study of binary neutron stars will be presented in a future paper.

#### A. Isolated stars

A standard test consists of evolving isolated, neutron stars and analyzing their oscillation modes. The frequencies of these modes can be computed independently by solving for the linearized perturbations in the Cowling approximation (i.e., fixed spacetime). The extent to which the frequencies obtained from our fully nonlinear evolution agree with those of the linearized code helps measure the correctness of our code.

We constructed initial data for our neutron stars using three different nuclear EoSs describing hot dense matter, all of them publicly available in [56], using MAGSTAR, part of LORENE [57]. The first one corresponds to the stiff EoS by Shen-Horowitz-Teige (SHT) [50] using the NL3 relativistic mean-field parametrization, the second one is by Lattimer-Swesty (LS) [51] with an incompressibility modulus  $K = 220$  MeV, representing a soft EoS, and the final one is the H. Shen (HS) [52] developed from relativistic mean-field theory with the TM1 parametrization. These equations of state have cold neutron star maximum gravitational masses of  $2.76M_\odot$ ,  $2.04M_\odot$ , and  $2.24M_\odot$ , respectively.

The simulations are performed on a numerical domain covering  $x^i \in [-60 \text{ km}, 60 \text{ km}]$  for the stars evolved in a fixed background, and it extends to  $x^i \in [-120 \text{ km}, 120 \text{ km}]$  when the spacetime is dynamical in order to prevent unphysical effects coming from the boundary. There are several refinement levels so that there is a grid covering the star with a resolution  $\Delta x = 250$  m. We evolve the system with a third order accurate, Runge-Kutta scheme with a time step given by  $\Delta t = 0.25\Delta x$ , satisfying the CFL condition.

#### 1. Cold stars

The cold star initial data are constructed assuming a very low temperature of  $T = 0.01$  MeV—well below the Fermi temperature of the star—and imposing  $\beta$ -equilibrium. An initial perturbation is introduced by increasing the initial temperature with respect to the temperature assumed during its construction to  $T = 0.05$  MeV. We choose a solution on the stable branch of nonrotating stars—near the maximum allowed mass—to coincide with that of Ref. [28] to facilitate comparison, corresponding to a central density  $\rho_c = 9.3 \times 10^{14} \text{ g/cm}^3$ .

We work in the Cowling approximation such that the metric is frozen at its initial profile so that we can compare easily with the results of perturbations from the linearized system. In particular, we Fourier transform the time-series data for the central density from the evolution code as shown in Fig. 3 for the star using the LS EoS. The results

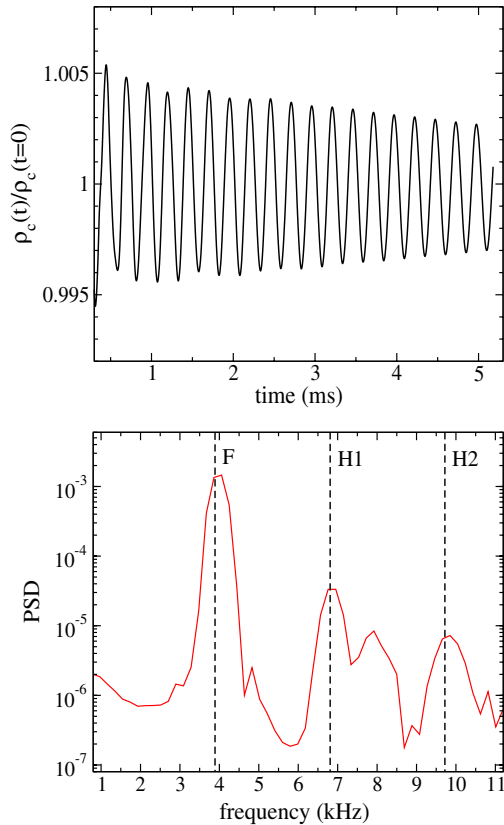


FIG. 3 (color online). Perturbed NS with the LS-K220 EoS in the Cowling approximation. *Top*: Central density of the star as a function of time. *Bottom*: The Fourier power spectral density as a function of frequency. Vertical dashed lines show the expected oscillation frequencies calculated by solving the linearized equations.

from linear analysis are shown as dashed lines, and these frequencies correspond quite well to the peaks of the Fourier power spectrum. The numerical values for the first three frequency modes  $f_i$  (i.e., the fundamental radial mode and the first two overtones) are summarized in Table I and are compared with the frequencies  $f_i^C$  computed either from perturbation theory (for fixed spacetimes) or with another full nonlinear code (for the dynamical spacetimes considered below). The maximum disagreement between these values is 2.5%, and generally below 1.5%. Note that, as happens with cold stars described by a polytropic EoS

(see for instance [58]), the mode frequencies are higher in fixed spacetimes than in dynamical ones.

With this same star, we can add an initial seed magnetic field. Here we add a poloidal field with a maximum strength of  $8 \times 10^{14}$  G, and evolve the full spacetime. In this case we transform the central value of both the density and the magnetic field, as shown in Fig. 4. Both spectra lead to the same frequencies. Because there are no published results from perturbation theory for the dynamical spacetime case, we are only able to compare the observed oscillation frequencies with the ones obtained from another independent, fully nonlinear code, Ref. [28], which also solves the general relativistic hydrodynamic equations with a neutrino leakage scheme.

## 2. Hot stars

Here we study a hot star, chosen to match one already studied in Ref. [28], also with a central density  $\rho_c = 9.3 \times 10^{14}$  g/cm<sup>3</sup>. In particular, we choose a star with constant entropy of  $s = 1$   $k_B$ /baryon in  $\beta$  equilibrium using the SHT EoS, leading to a temperature of  $T \approx 30$  MeV at the center, which decreases towards the surface. We let discretization error serve as the only perturbation.

We evolve in the Cowling approximation by freezing the spacetime in order to compare the normal frequencies with the ones obtained from the linearized system. The star is given an initial, poloidal, magnetic field with maximum strength  $5 \times 10^{14}$  G, and we allow the star to cool via neutrino emission as described by the leakage scheme. The central values of the density and the magnetic field are plotted in Fig. 5. The frequencies, summarized in Table I, are in good agreement with those calculated in Ref. [28].

We also display the neutrino luminosities for each species in Fig. 6. During the first millisecond, both the  $\nu_e$  and  $\bar{\nu}_e$  luminosities vary significantly as the star achieves its new equilibrium configuration for the chosen numerical grid. In particular, we find a mixing of the neutron-rich matter and an increase of the temperature near the stellar surface due to (i) the fluid evolution outside the star (i.e., with thermal ejections of stellar material, shock heating, and accretion of the atmosphere), (ii) the internal normal oscillations of the star, and (iii) numerical diffusion. These effects are enough to drive the  $Y_e$  away from its original  $\beta$ -equilibrium

TABLE I. Mode frequencies of the oscillations of a NS with  $\rho_c = 9.3 \times 10^{14}$  g/cm<sup>3</sup>. We compute the first three frequencies (i.e., the fundamental radial mode and the two first overtones)  $f_i$  and compare with frequencies  $f_i^C$  from either a linearized code (fixed spacetime) or from another nonlinear code [28] (dynamic spacetime). Note that in the last two cases the star contains a poloidal magnetic field and the oscillation of the central magnetic field matches that of the fluid density (see the bottom panels of Figs. 4 and 5).

Model	Metric	$M[M_\odot]$	$R$ [km]	$s[k_B]$	$B_c$ [G]	$f_1$ [KHz]	$f_1^C$ [KHz]	$f_2$ [KHz]	$f_2^C$ [KHz]	$f_3$ [KHz]	$f_3^C$ [KHz]
SHT	Fixed	2.73	13.90	0	0	3.54	3.49	5.87	5.86	8.34	8.24
LS-K220	Fixed	1.69	12.36	0	0	3.96	3.89	6.84	6.81	9.95	9.72
LS-K220	Dynamic	1.69	12.36	0	$5 \times 10^{14}$	2.37	2.39	6.07	6.09	9.23	9.41
SHT	Fixed	2.74	14.14	1	$5 \times 10^{14}$	3.53	3.42	5.90	5.73	8.32	8.01

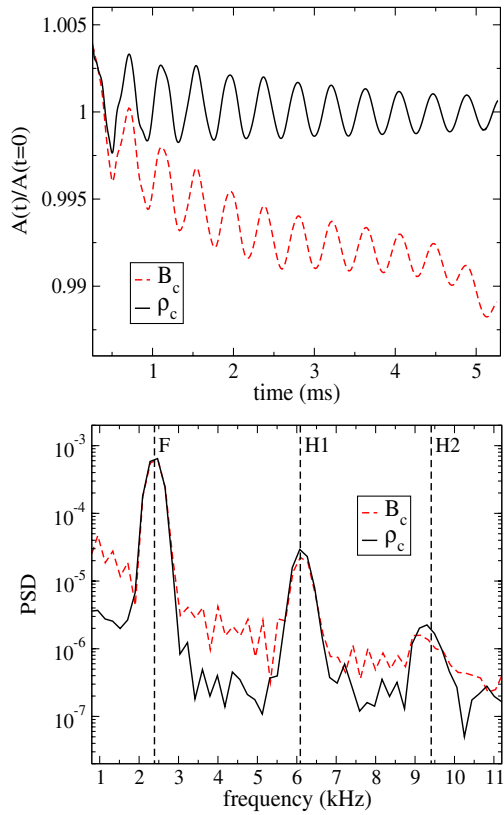


FIG. 4 (color online). Perturbed, magnetized NS with the LS-K220 EoS in a dynamic spacetime. *Top*: The (normalized) central density of the star and central magnetic field strength as a function of time. The initial star has a purely poloidal magnetic field. *Bottom*: The Fourier power spectral density as a function of frequency. Vertical dashed lines show the computed oscillation frequencies obtained by using another full nonlinear evolution code.

configuration and to produce a slow and steady rise of all the neutrino luminosities after  $t \approx 2$  ms. Before the steady rise, the  $\nu_e$ ,  $\bar{\nu}_e$ , and  $\nu_x$  luminosities are  $\approx 3 \times 10^{51}$  erg/s,  $\approx 2 \times 10^{51}$  erg/s, and  $\approx 0.2 \times 10^{51}$  erg/s, respectively. Here, we include all four heavy-lepton species in the  $\nu_x$  luminosity.

Our results show a much lower neutrino luminosity than those of [28] for the same model, who at the stationary state have luminosities of  $\approx 30 \times 10^{51}$  erg/s,  $\approx 70 \times 10^{51}$  erg/s, and  $\approx 15 \times 10^{51}$  erg/s, for  $\nu_e$ ,  $\bar{\nu}_e$ , and  $\nu_x$ , respectively. However, high resolution (50 m) tests with this same stellar configuration in GR1D both with this identical leakage scheme [39] and with a two-moment closure neutrino transport scheme [59] suggest that our luminosities are reasonable and indicate that these large differences may arise due to the treatment of low density regions, which seems to be crucial in this particular problem. With GR1D's leakage scheme we achieve luminosities at the stationary state of  $\approx 0.8 \times 10^{51}$  erg/s,  $\approx 0.4 \times 10^{51}$  erg/s, and  $\approx 0.7 \times 10^{51}$  erg/s. With GR1D's two-moment neutrino transport, we determine hydrostatic neutrino

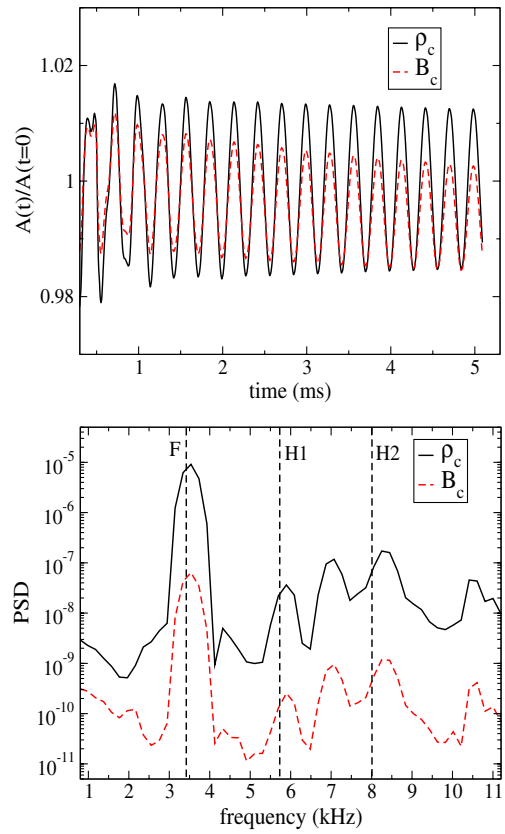


FIG. 5 (color online). Perturbed, magnetized hot NS with the SHT EoS in a fixed spacetime. *Top*: The (normalized) central density of the star and central magnetic field strength as a function of time. *Bottom*: The Fourier power spectral density as a function of frequency. Leakage results for this star are shown Fig. 6.

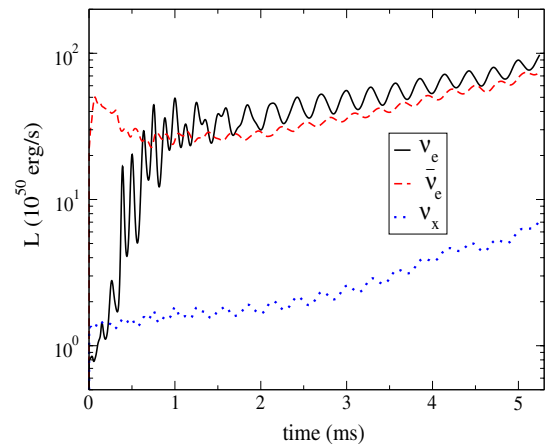


FIG. 6 (color online). Perturbed, magnetized hot NS with the SHT EoS in a fixed spacetime. The luminosities of the different neutrino species are displayed as a function of time. Notice that, after the initial transient of  $\approx 1$  ms, all luminosities rise steadily. We attribute this to the increasing temperature near the star's surface due mainly to numerical diffusion and to the evolution of the atmosphere.

luminosities of  $\approx 0.3 \times 10^{51}$  erg/s,  $\approx 0.5 \times 10^{51}$  erg/s, and  $\approx 0.8 \times 10^{51}$  erg/s for  $\nu_e$ ,  $\bar{\nu}_e$ , and  $\nu_x$ , respectively. We see lower luminosities in spherical symmetry because of the reduced numerical diffusion and the inability to capture convection in the atmosphere region.

We are able to attribute all the observed differences in the neutrino luminosities in our three-dimensional simulations and the GR1D simulations to the outer  $\approx 1$ – $2$  km of the star. Interior to this, the leakage quantities are initially essentially identical and vary only slightly. In the interior region, the grey radial luminosity determined with GR1D’s leakage scheme is in very good agreement with the energy summed neutrino luminosity from GR1D’s neutrino transport. The outer regions are much harder to accurately capture with a leakage scheme as both the neutrinospheres and the region where the dominant neutrino leakage contributions transition from diffusion to free emission, occur very close to the steep density gradient of the neutron star’s surface. For this reason, we express caution when interpreting these luminosities.

In an effort to better understand the effects of both magnetic field and neutrino cooling, we study the evolution of a hot (12 MeV), dense ( $5.6 \times 10^{15}$  g/cm<sup>3</sup>), rapidly spinning (1500 Hz) neutron star using the HS EoS. For such a large central density and mass (baryonic mass  $2.1 M_\odot$ ), the star is unstable to collapse providing a dynamic solution to study. We consider the star with no magnetic field and contrast it when the star is given a very strong magnetic field. We consider two magnetized cases parametrized by a maximum initial magnetic field strength of  $4.1 \times 10^{16+n}$  with  $n = 0, 2$ . The low value ( $n = 0$ ) could arise dynamically in the hypermassive neutron star resulting from binary merger [18,30,32,60]. The high value ( $n = 2$ ), while unrealistically high, allows us to explore strong magnetic fields which can have a significant effect on the pressure and structure of the star and, consequently, on the neutrino production. Notice that we neglect these effects in the construction of the initial data, adding the magnetic field to the star as a “seed.” Nevertheless, these evolutions serve primarily to explore some of the possible differences and the robustness of the code, in addition to assessing at which level such magnetizations can affect the dynamics.

Figure 7 shows various quantities as functions of time for both unmagnetized and magnetized evolutions. In Fig. 8, we show plots of certain fields at a late time during the collapse. As shown in the figure, only unreasonably high magnetizations significantly changes the neutrino production. Magnetic fields do not couple strongly to neutrino cooling in realistic scenarios and instead affect neutrino results through effects to stellar structure and temperature. Notice however, that in binary mergers the magnetic field can significantly affect the distribution of material and the transport of angular momentum of the merger remnant. And these effects can, in turn, impact neutrino production and luminosity.

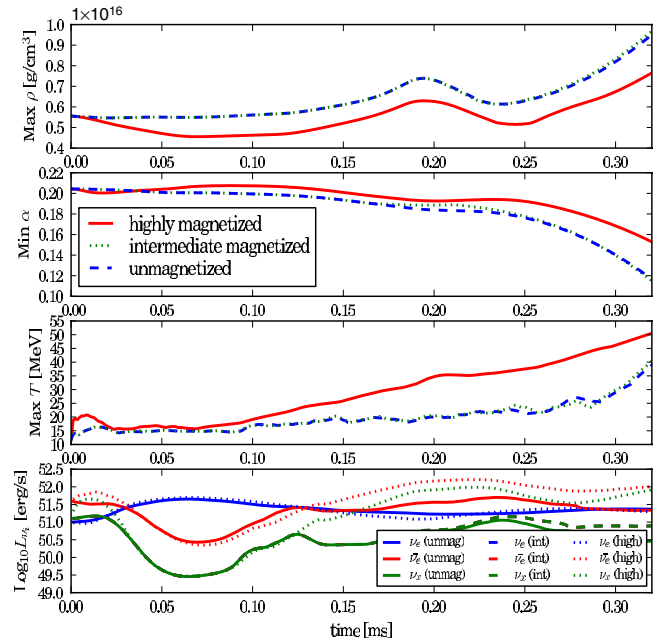


FIG. 7 (color online). Hot, dense, rapidly rotating star. The maximum density, minimum lapse, maximum temperature, and total neutrino luminosities are shown versus time for the collapse of an unstable, hot, dense, rapidly rotating star. Three evolutions are contrasted, one with no magnetization (blue dashed) one with a very large initial field (red solid), and one with an intermediate magnetization (green dotted). The intermediate star is nearly identical to the unmagnetized star except for its late-stage neutrino luminosity. The magnetized star has an initial magnetic field with a maximum of  $4.1 \times 10^{16}$  G whereas as the most magnetized case begins with a field one hundred times larger. Pictures of the star in its late stage are shown in Fig. 8.

## B. Binary neutron stars

The inspiral and merger of two neutron stars is a significant test of a code such as this. The inherent asymmetry of the problem tends to “excite” many, if not all, terms in the equations. Resolving both the motion of two compact objects as well as the large gradients at their surfaces requires significant resources. The merger itself is a very dynamic process with a large range of densities.

We consider here just the late stage (roughly the last 4.5 orbits) of a single binary evolved with just a single EoS. We have evolved this binary with three different resolutions and find convergent results. The preliminary results presented here arise from our highest resolution which has a finest grid spacing in all directions of 460 m. This resolution is enough to capture the main aspects of the dynamics, though we note higher resolutions are needed for a more detailed study of the system.

We include neutrino cooling during the inspiral as a test of our leakage scheme even though for times much before merger one expects very little emission. Above we show that the computation of the optical depth tracks the stars appropriately in Fig. 2. Here we show results for a binary

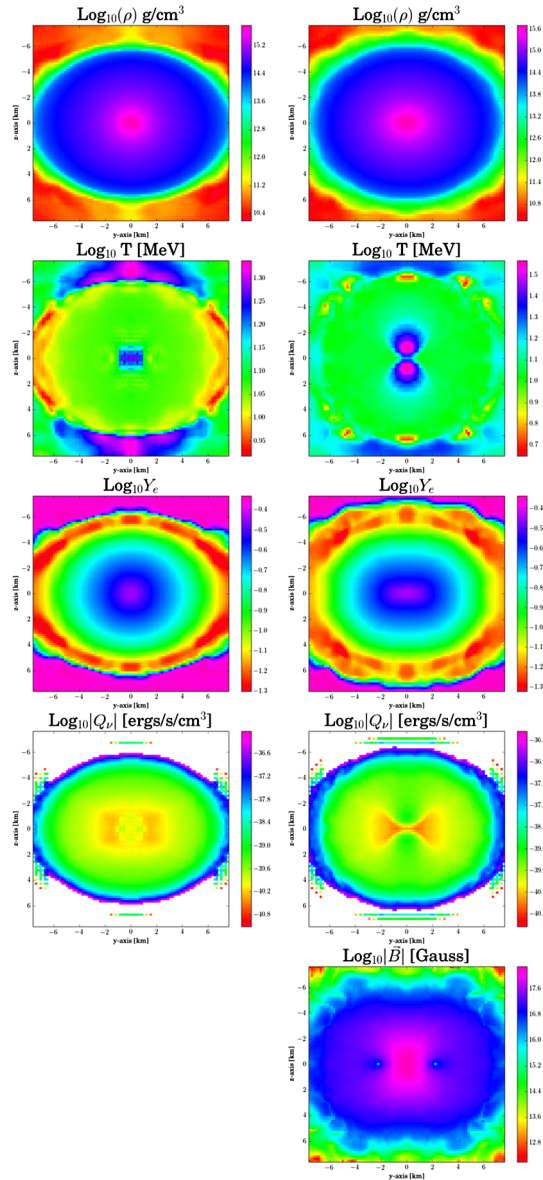


FIG. 8 (color online). Hot, dense, rapidly rotating star. Snapshots of various quantities on a meridional plane are shown at  $t = 0.25$  ms for the same unmagnetized star (left) and highly magnetized star (right) as shown in Fig. 7. From top to bottom are shown the density, temperature, electron fraction, total neutrino emissivity, and the magnitude of the magnetic field. The square central region in the temperature (and concomitantly the emissivity) of the unmagnetized star appears related to the squared boundaries.

constructed using LORENE with the HS EoS for which each star has baryonic mass  $M_B = 1.49M_\odot$  and equatorial radius  $R \approx 14.5$  km and temperature 0.01 MeV. The binary has an initial separation  $a = 45$  km, a total ADM mass  $M_{\text{ADM}} = 2.74M_\odot$ , and an orbital angular velocity  $\Omega = 1796 \text{ rad s}^{-1}$ . The electron fraction is set so that the stars are initially in  $\beta$  equilibrium. Neutron star binaries are expected to be rather cool, but higher temperatures will be reached during merger. We have run this binary at three

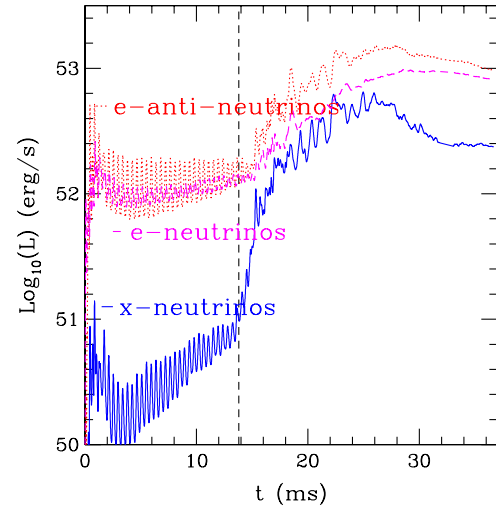


FIG. 9 (color online). Neutrino luminosities for the merger of a binary neutron star system. The dashed line at  $t = 13.8$  ms denotes when the stars first touch. Note the rapid growth of the luminosities for all species after this time. Snapshots of the binary at a few of these late times are shown in Fig. 10.

resolutions and find that the hydrodynamical and gravitational dynamics are convergent.

In Fig. 9 we show the integrated luminosities for each neutrino species as a function of time. After an initial transient, the luminosities for both electron-neutrinos and electron-antineutrinos become roughly comparable while the heavy-lepton neutrino types are much less luminous. The large oscillations in the luminosities are an unfortunate artifact of an inconsistency between the temperature provided to the initial data solver and that provided to the evolution code. This inconsistency acts as a very large perturbation to the binary resulting in oscillations in the initial density that naturally induce oscillations in the other fields, but otherwise does not affect the dynamics of the orbiting stars. A simulation such as this assumes no symmetries and therefore places no restrictions on the dynamical physical modes that the merger can excite. Because an evolution of the full, three-dimensional domain requires close to 100 000 CPU hours, we defer for our follow-up work simulations with better initial data for which preliminary results show much smaller oscillations.

Once the stars touch, the temperature and concomitant neutrino luminosity increase for all species. Interestingly, the most dominant radiative neutrino flavor is the electron antineutrino. This dominance has already been observed in other binary neutron star mergers [23,25] and also neutron star-black hole mergers [26], and is due to neutron rich material being shock heated and decompressed [61]. This neutron rich, low density, hot material is initially far below the new  $\beta$ -equilibrium value of  $Y_e$  and will preferentially emit electron antineutrinos until it is reestablished. This can be seen by inspection of the bottom row on the right side of Fig. 10, which shows the lepton number matter source term.

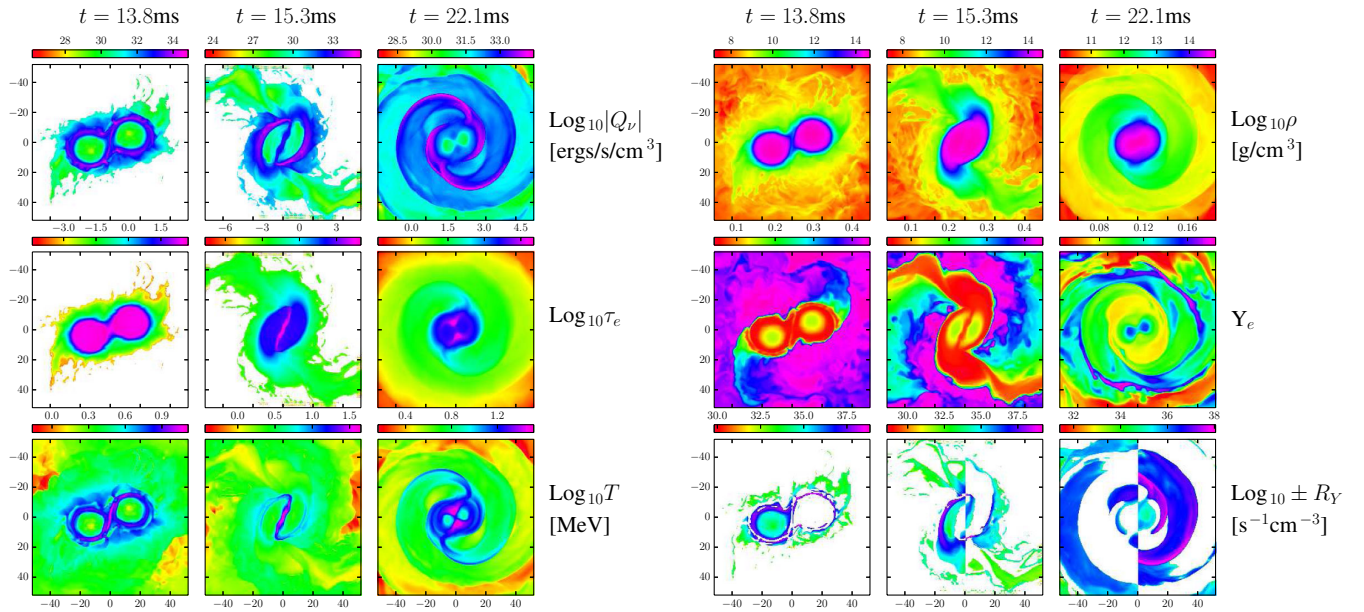


FIG. 10 (color online). Snapshots of the binary merger looking down upon the orbital plane. The total neutrino emissivity, electron-neutrino optical depth, and temperature are shown at three times ( $t = 13.8$  ms,  $15.3$  ms, and  $22.1$  ms) increasing from left to right. For the plots of  $R_Y$ , the right side ( $x > 0$ ) of the plot shows positive values (net electron antineutrino emission) whereas the left side ( $x < 0$ ) shows negative values (net electron neutrino emission). The first time shows when the stars first touch and the middle time shows the system when the temperature reaches its maximum. The final column shows the remnant at  $t = 22.1$  ms, a while after merger when it has settled down to a rotating, hot “dumb-bell” with spiral arms of emissive material. The luminosities for each neutrino species as functions of time are shown in Fig. 9.

On the left half ( $x < 0$ ) of each panel we show (in color-log scale) regions of net positive lepton number emission and mask out regions of net negative lepton number emission. While on the right half ( $x > 0$ ) we only show regions of net negative lepton number emission and mask out positive lepton number emission. In the rightmost column, at  $22.1$  ms, the largest contribution to the antineutrino emission (again,  $x > 0$ ) occurs at the leading edges of the tidal tails where  $T \approx 15$  MeV,  $\rho \approx 10^{12}$  g cm $^{-3}$ , and  $Y_e \approx 0.1$ . This can be understood by noting that for this temperature, density, and EoS, we have that  $Y_{e,\beta\text{-equil}} \approx 0.29$ , significantly above the instantaneous value of  $Y_e \approx 0.1$ . In contrast, the dominant region of electron neutrino number emission, albeit small, is outside of the dominant tidal tail region (for radii  $\gtrsim 40$  km). This matter is colder and less dense, characterized by  $T \approx 2.5$  MeV,  $\rho \approx (1-2) \times 10^{11}$  g cm $^{-3}$ , and  $Y_e \approx 0.1-0.15$ . Since the optical depth is low for this region, the equilibrium  $Y_e$  that the system will tend to is the  $Y_e$  where neutrino number emission balances antineutrino number emission rather than the  $\beta$ -equilibrium value, which assumes there exists a population of trapped neutrinos and antineutrinos that can undergo capture on neutrons and protons. For these conditions,  $Y_{e,\text{rate equil}} \approx 0.05$ , hence we generally expect dominant electron neutrino emission.

Our results are largely consistent with past work for similar mass binaries, indicating that despite differences in the adopted approaches, simulations predict a rather robust behavior of neutrino luminosities  $\approx 10^{53}$  ergs s $^{-1}$ . The

dominant contribution is provided by electron antineutrinos, followed with a somewhat lower luminosity by electron neutrinos. The heavy-lepton neutrino luminosity is roughly half those of the light species for the roughly 15 ms immediately after the merger, but decays considerably afterwards as the disk settles and cools. The faster decline of the heavy-lepton luminosities relative to the electron type species is due to the different emission processes. Heavy-lepton neutrino emission is dominated by electron-positron annihilation, which has a stronger temperature dependence than charged-current processes which dominate the electron-type neutrino emission.

Snapshots corresponding to the merging binary are shown in Fig. 10, illustrating, at representative times after merger, the behavior of energy sink ( $Q_\nu$ ), electron neutrino optical depth ( $\tau_e$ ), temperature ( $T$ ), density ( $\rho$ ), electron fraction ( $Y_e$ ), and lepton source ( $R_Y$ ). This figure illustrates several important features. First, the energy sink, lepton sources and temperature are tied to surface, shearing regions, and tidal tails. Second, the optical depth tracks, as expected, the density behavior. Third, the electron fraction shows regions above and below beta equilibrium that induce stronger production of electron neutrinos and antineutrinos. Fourth, the merger gives rise to a significant increase in the temperature, reaching a peak value of roughly 45 MeV. Notice that for this low total-mass binary, the HMNS does not show indications of impending collapse for the time of this simulation (roughly 25 ms

after merger) implying a longer lived remnant. We defer to future work a systematic analysis of the dependence on total mass, EoS and magnetic field effects on the onset of black hole formation, as well as other properties of the merger remnant, mass outflow, and resulting nucleosynthesis.

#### IV. CONCLUSIONS

We have described our implementation of a general relativistic, magnetohydrodynamics code that uses realistic, tabulated equations of state as well as accounts for neutrino cooling through a leakage scheme. In particular, we have presented a new method to obtain the optical depth along with a test illustrating that the optical depth is accurately integrating the opacity [62]. With this implementation we have studied the effects magnetic fields can have on the collapse of a rapidly spinning, hot, dense star with neutrino cooling. We also presented first applications of this code to a binary neutron star system obtaining, in particular, the neutrino luminosity induced by the merger. For both single

star cases and binaries, the calculated values are in agreement with recent work [23,28] as well as with results obtained with a core collapse code [39].

#### ACKNOWLEDGMENTS

It is a pleasure to thank C. Ott, T. Janka, S. Rosswog, L. Caballero, F. Galeazzi, and A. Burrows for discussions about neutrino effects and techniques, as well as our long-time collaborators E. Hirschmann, P. Motl, and M. Ponce. This work was supported by the NSF under Grants No. PHY-0969827 and No. PHY-1308621 (LIU) and No. PHY-0969811 and No. PHY-1308727 (BYU), NASA's ATP program through Grant No. NNX13AH01G, NSERC through a Discovery Grant (L. L.), and CIFAR (L. L.). C. P. acknowledges support by the Jeffrey L. Bishop Fellowship. Research at Perimeter Institute is supported through Industry Canada and by the Province of Ontario through the Ministry of Research and Innovation. Computations were performed at XSEDE and Scinet.

- 
- [1] B. P. Abbott *et al.* (LIGO Scientific Collaboration), *Rep. Prog. Phys.* **72**, 076901 (2009).
  - [2] T. Accadia *et al.*, *Classical Quantum Gravity* **28**, 114002 (2011).
  - [3] K. Somiya (KAGRA Collaboration), *Classical Quantum Gravity* **29**, 124007 (2012).
  - [4] J. S. Read, C. Markakis, M. Shibata, K. Uryū, J. D. Creighton, and J. Friedman, *Phys. Rev. D* **79**, 124033 (2009).
  - [5] B. D. Lackey, K. Kyutoku, M. Shibata, P. R. Brady, and J. L. Friedman, *Phys. Rev. D* **85**, 044061 (2012).
  - [6] J. S. Read, L. Baiotti, J. D. E. Creighton, J. L. Friedman, B. Giacomazzo, K. Kyutoku, C. Markakis, L. Rezzolla, M. Shibata, and K. Taniguchi, *Phys. Rev. D* **88**, 044042 (2013).
  - [7] E. Barausse, C. Palenzuela, M. Ponce, and L. Lehner, *Phys. Rev. D* **87**, 081506 (2013).
  - [8] C. Palenzuela, E. Barausse, M. Ponce, and L. Lehner, *Phys. Rev. D* **89**, 044024 (2014).
  - [9] M. Shibata, K. Taniguchi, H. Okawa, and A. Buonanno, *Phys. Rev. D* **89**, 084005 (2014).
  - [10] E. Berger, [arXiv:1311.2603](https://arxiv.org/abs/1311.2603).
  - [11] C. Spiering, [arXiv:1402.2096](https://arxiv.org/abs/1402.2096).
  - [12] M. D. Duez, F. Foucart, L. E. Kidder, C. D. Ott, and S. A. Teukolsky, *Classical Quantum Gravity* **27**, 114106 (2010).
  - [13] K. Hotokezaka, K. Kyutoku, H. Okawa, M. Shibata, and K. Kiuchi, *Phys. Rev. D* **83**, 124008 (2011).
  - [14] Z. B. Etienne, Y. T. Liu, S. L. Shapiro, and T. W. Baumgarte, *Phys. Rev. D* **79**, 044024 (2009).
  - [15] S. Chawla, M. Anderson, M. Besselman, L. Lehner, S. L. Liebling, P. M. Motl, and D. Neilsen, *Phys. Rev. Lett.* **105**, 111101 (2010).
  - [16] F. Foucart, M. D. Duez, L. E. Kidder, and S. A. Teukolsky, *Phys. Rev. D* **83**, 024005 (2011).
  - [17] L. Rezzolla, L. Baiotti, B. Giacomazzo, D. Link, and J. A. Font, *Classical Quantum Gravity* **27**, 114105 (2010).
  - [18] M. Anderson, E. W. Hirschmann, L. Lehner, S. L. Liebling, P. M. Motl, D. Neilsen, C. Palenzuela, and J. Tohline, *Phys. Rev. Lett.* **100**, 191101 (2008).
  - [19] Y. T. Liu, S. L. Shapiro, Z. B. Etienne, and K. Taniguchi, *Phys. Rev. D* **78**, 024012 (2008).
  - [20] B. Giacomazzo, L. Rezzolla, and L. Baiotti, *Mon. Not. R. Astron. Soc.* **399**, L164 (2009).
  - [21] Z. B. Etienne, V. Paschalidis, and S. L. Shapiro, *Phys. Rev. D* **86**, 084026 (2012).
  - [22] C. Palenzuela, L. Lehner, M. Ponce, S. L. Liebling, M. Anderson, D. Neilsen, and P. Motl, *Phys. Rev. Lett.* **111**, 061105 (2013).
  - [23] Y. Sekiguchi, K. Kiuchi, K. Kyutoku, and M. Shibata, *Prog. Theor. Phys.* **12**, 01A304 (2012).
  - [24] K. Kiuchi, Y. Sekiguchi, K. Kyutoku, and M. Shibata, *Classical Quantum Gravity* **29**, 124003 (2012).
  - [25] Y. Sekiguchi, K. Kiuchi, K. Kyutoku, and M. Shibata, *Phys. Rev. Lett.* **107**, 051102 (2011).
  - [26] M. B. Deaton, M. D. Duez, F. Foucart, E. O'Connor, C. D. Ott, L. E. Kidder, C. D. Muhlberger, M. A. Scheel, and B. Szilagy, *Astrophys. J.* **776**, 47 (2013).
  - [27] J. Kaplan, C. Ott, E. O'Connor, K. Kiuchi, L. Roberts *et al.*, [arXiv:1306.4034](https://arxiv.org/abs/1306.4034).
  - [28] F. Galeazzi, W. Kastaun, L. Rezzolla, and J. A. Font, *Phys. Rev. D* **88**, 064009 (2013).
  - [29] V. Paschalidis, Z. B. Etienne, and S. L. Shapiro, *Phys. Rev. D* **86**, 064032 (2012).

- [30] D. J. Price and S. Rosswog, *Science* **312**, 719 (2006).
- [31] B. Giacomazzo, L. Rezzolla, and L. Baiotti, *Phys. Rev. D* **83**, 044014 (2011).
- [32] M. Obergaulinger, M. A. Aloy, and E. Müller, *Astron. Astrophys.* **515**, A30 (2010).
- [33] J. Zrake and A. I. MacFadyen, *Astrophys. J.* **769**, L29 (2013).
- [34] H. R. Takahashi, K. Ohsuga, Y. Sekiguchi, T. Inoue, and K. Tomida, *Astrophys. J.* **764**, 122 (2013).
- [35] M. Shibata and Y. Sekiguchi, *Prog. Theor. Phys.* **127**, 535 (2012).
- [36] K. Hotokezaka, K. Kyutoku, M. Tanaka, K. Kiuchi, Y. Sekiguchi, M. Shibata, and S. Wanajo, *Astrophys. J.* **778**, L16 (2013).
- [37] M. H. Ruffert, H. T. Janka, and G. Schaefer, *Astron. Astrophys.* **311**, 532 (1996).
- [38] S. Rosswog and M. Liebendoerfer, *Mon. Not. R. Astron. Soc.* **342**, 673 (2003).
- [39] E. O'Connor and C. D. Ott, *Classical Quantum Gravity* **27**, 114103 (2010).
- [40] M. Liebendoerfer, S. Whitehouse, and T. Fischer, *Astrophys. J.* **698**, 1174 (2009).
- [41] D. Neilsen, L. Lehner, C. Palenzuela, E. W. Hirschmann, S. L. Liebling, P. M. Motl, and T. Garrett, *Proc. Natl. Acad. Sci. U.S.A.* **108**, 12641 (2011).
- [42] D. Neilsen, E. W. Hirschmann, and R. S. Millward, *Classical Quantum Gravity* **23**, S505 (2006).
- [43] S. L. Liebling, [arXiv:1002.2217](https://arxiv.org/abs/1002.2217).
- [44] T. Nakamura, K. Oohara, and Y. Kojima, *Prog. Theor. Phys. Suppl.* **90**, 1 (1987).
- [45] M. Shibata and T. Nakamura, *Phys. Rev. D* **52**, 5428 (1995).
- [46] T. W. Baumgarte and S. L. Shapiro, *Phys. Rev. D* **59**, 024007 (1999).
- [47] M. Campanelli, C. O. Lousto, P. Marronetti, and Y. Zlochower, *Phys. Rev. Lett.* **96**, 111101 (2006).
- [48] S. L. Liebling, L. Lehner, D. Neilsen, and C. Palenzuela, *Phys. Rev. D* **81**, 124023 (2010).
- [49] A. Dedner, F. Kemm, D. Kröner, C.-D. Munz, T. Schnitzer, and M. Wesenberg, *J. Comput. Phys.* **175**, 645 (2002).
- [50] G. Shen, C. J. Horowitz, and S. Teige, *Phys. Rev. C* **83**, 035802 (2011).
- [51] J. M. Lattimer and F. Douglas Swesty, *Nucl. Phys.* **A535**, 331 (1991).
- [52] H. Shen, H. Toki, K. Oyamatsu, and K. Sumiyoshi, *Astrophys. J. Suppl. Ser.* **197**, 20 (2011).
- [53] Suggested by Philip Chang.
- [54] Pointed out to us by Ian Hawke.
- [55] H. Zhao, *Math. Comput.* **74**, 603 (2005).
- [56] C. D. Ott, <http://www.stellarcollapse.org/microphysics>.
- [57] LORENE, home page <http://www.lorene.obspm.fr/>.
- [58] J. A. Font, T. Goodale, S. Iyer, M. Miller, L. Rezzolla, E. Seidel, N. Stergioulas, W.-M. Suen, and M. Tobias, *Phys. Rev. D* **65**, 084024 (2002).
- [59] E. O'Connor and C. D. Ott, *Astrophys. J.* **762**, 126 (2013).
- [60] J. Zrake and A. I. MacFadyen, [arXiv:1303.1450](https://arxiv.org/abs/1303.1450).
- [61] M. Ruffert, H.-T. Janka, K. Takahashi, and G. Schaefer, *Astron. Astrophys.* **319**, 122 (1997).
- [62] At the completion of this work, an independent, related approach has been presented in [63].
- [63] A. Perego, E. Gafton, R. Cabezón, S. Rosswog, and M. Liebendoerfer, [arXiv:1403.1297](https://arxiv.org/abs/1403.1297).